Chirality-dependent pathway interference in optimal enantioselective state transfer

Yu Guo(郭裕)[1] and Li-Bao Fan(樊丽宝)[1*]

[1]Hunan Provincial Key Laboratory of Flexible Electronic Materials Genome Engineering, School of Physics and Electronic Science, Changsha University of Science and Technology, Changsha 410114, China

Abstract

We theoretically study enantioselective state transfer (ESST) in a reduced four-level rotational model of a chiral molecule. The cyclic three-level description is reliable only when the microwave bandwidth remains well below the detunings to nearby dipole-allowed rotational transitions. When the bandwidth becomes comparable to the detuning of the nearest relevant additional state, this state can participate in the dynamics, requiring a four-level description. Using a constrained multiobjective quantum optimal-control method, we design microwave control fields in the narrow-band three-level and broadband four-level regimes. The resulting optimized fields achieve final discrimination degrees above 0.999 under four-level propagation in both regimes, while direct four-level optimization permits shorter-duration control by explicitly accounting for transient fourth-state participation. To reveal the underlying coherent mechanism, the transition amplitudes are decomposed into even- and odd-a pathway groups. The even-a contribution is common to the two enantiomers, whereas the odd-a contribution changes sign, resulting in constructive interference for one enantiomer and destructive interference for the other. Lindblad simulations further show that the four-level optimized control fields exhibit enhanced robustness against rotational relaxation owing to their shorter control durations. These results show that broadband four-level optimization can enable faster ESST with improved robustness against dissipative relaxation while preserving the even/odd-a pathway-interference mechanism.

Keywords: Chiral molecules; Enantioselective state transfer; Quantum optimal control

PACS: 42.50.-p, 42.50.Dv, 33.20.Bx

1. Introduction

Molecular chirality provides a natural setting for phase-sensitive quantum control because two enantiomers have the same field-free energy spectrum in an achiral environment but differ in the relative signs of their molecular-frame transition dipole components. This symmetry property underlies optical activity as well as spectroscopic and electric-dipole-based probes of handedness [1–11]. In the rotational domain, the sign difference of a transition-dipole component can be converted into a controllable quantum phase,

*Corresponding author. E-mail: libaofanxv@foxmail.com

allowing microwave fields to distinguish otherwise degenerate left- and right-handed enantiomers [12–14]. Coherent microwave control can therefore encode molecular handedness in the interference of transition amplitudes.

A particularly transparent setting is provided by a cyclic three-level configuration. Three rotational states are connected by mutually orthogonal a-, b-, and c-type transitions, and the product of the three transition dipoles changes sign between the two enantiomers [12–15]. In such a loop, different excitation pathways can interfere constructively for one enantiomer and destructively for the other. This idea appeared in early proposals for cyclic population transfer in broken-symmetry quantum systems and related coherent enantioselective control schemes [13–16] and has since been developed into microwave three-wave-mixing spectroscopy and state-selective enantiomeric enrichment [3,4,17–20]. Recently, near-complete rotational-state chiral selection was experimentally demonstrated in 1-indanol, with an enantiomer-specific state-transfer efficiency above 92%, corresponding to a target-state enantiomeric composition of approximately 96 : 4 [21]. Further theoretical work has pursued several routes to ESST, including shortcut-to-adiabaticity schemes [22,23], three-mode and two-path interference protocols [24,25], pulse-area and analytically designed pulse sequences [26–28], effective two-level and SU(2)-based formulations [29,30], pump-control schemes [31], dissipative pumping based on a handedness-dependent dark state [32], and controllability analyses in degenerate rotational manifolds [33].

Material-based enantiomer separation has also advanced rapidly, with homochiral metal-organic framework and covalent organic framework membranes enabling efficient enantioselective separation [34, 35]. Complementary to these material-based approaches, ESST maps molecular handedness onto internal rotational states. Once the L- and R-handed enantiomers occupy different states, state-selective operations can act differently on them. This provides a basis for state-specific enantiomeric enrichment, enantiomer separation, and enantiomeric-excess determination [4,17–19,22,25]. For practical use, such protocols should be both fast and robust. Recent studies on minimum-time chiral resolution and energy-time costs of ESST further highlight the importance of speed and resource efficiency in enantioselective control [36,37]. However, shortening the control time inevitably broadens the microwave spectrum. When the bandwidth becomes comparable to the detunings from nearby rotational transitions, states outside the nominal cyclic subsystem may be off-resonantly driven. This implies that broadband ESST should, in general, be designed in an enlarged Hilbert space including the relevant nearby rotational states. Here, the nearest fourth rotational state, identified by the smallest detunings of its dipole-allowed transitions from the applied control frequencies, is included as a minimal extension of the cyclic three-level model, allowing us to quantify the validity of the three-level approximation and to design broadband control fields. Four-level ESST has also been considered in a model containing two cyclic subloops, for which an analytical pump-control protocol was developed [31]. Unlike that configuration, the present four-level extension describes the bandwidth-dependent participation of a nearby off-resonant rotational state.

Quantum optimal control theory (QOCT) provides a systematic route to designing microwave control fields in such multilevel settings. Its central idea is to search for time-dependent control fields that

maximize a desired quantum objective under physical constraints [38–47]. Monotonically convergent and constrained algorithms have been developed in both time and frequency domains [48–57]. Here, we use a constrained multiobjective QOCT method to optimize the three microwave control fields simultaneously. In the narrow-band regime, the optimization is performed in the cyclic three-level model. In the broadband regime, the optimization is carried out directly in the four-level model so that transient fourth-state participation can be included during the search. To understand the optimized dynamics, we further develop an even/odd-a pathway analysis, in which the labels "even-a" and "odd-a" refer to pathway contributions containing even and odd numbers of a-type interactions whose signs reverse between the two enantiomers, respectively. This analysis separates the transition amplitude into pathway groups that either remain invariant or change sign under the enantiomeric sign reversal.

In this work, we establish the bandwidth-dependent validity of the isolated cyclic three-level approximation and identify the regime in which the nearest additional rotational state must be included explicitly. We further show that ESST in both the narrow-band and broadband regimes arises from constructive and destructive interference between the even-a and odd-a pathway groups, rather than from the dominance of one pathway group over the other. We also demonstrate that direct four-level optimization can permit shorter control durations, thereby enabling faster ESST and improving robustness against dissipative relaxation.

2. Theoretical model and method

We introduce the four-level dynamical model and the constrained multiobjective QOCT method used in this work. As shown in Fig. 1(a), three mutually orthogonal microwave control fields are optimized to drive the chiral molecule. Figure 1(b) shows the corresponding four-level coupling scheme, where the cyclic three-level ESST subsystem is embedded in a minimally enlarged Hilbert space by including the nearest relevant fourth rotational state coupled by the same microwave fields. This four-level embedding provides a minimal model for examining how nearby off-resonant transitions affect broadband ESST and for designing broadband control fields beyond the isolated three-level approximation.

2.1. Four-level chiral-molecule model

We consider four rotational states of a chiral molecule, $\{|1\rangle, |2\rangle, |3\rangle, |4\rangle\}$. The states $|1\rangle$, $|2\rangle$, and $|3\rangle$ form the cyclic ESST subsystem, which is driven by three mutually orthogonal microwave control fields $E_a(t)$, $E_b(t)$, and $E_c(t)$, associated with the a-, b-, and c-type transitions of the cyclic subsystem, respectively. The fourth state $|4\rangle$ is included as the nearest additional rotational state. In addition to the cyclic ESST transitions, the control field $E_a(t)$ couples $|3\rangle \leftrightarrow |4\rangle$, whereas the control field $E_c(t)$ couples $|1\rangle \leftrightarrow |4\rangle$. For the two enantiomers, we use a phase convention in which the a-type dipoles change sign, whereas the b- and c-type dipoles are the same. With this convention, the Hamiltonian for the χ-handed

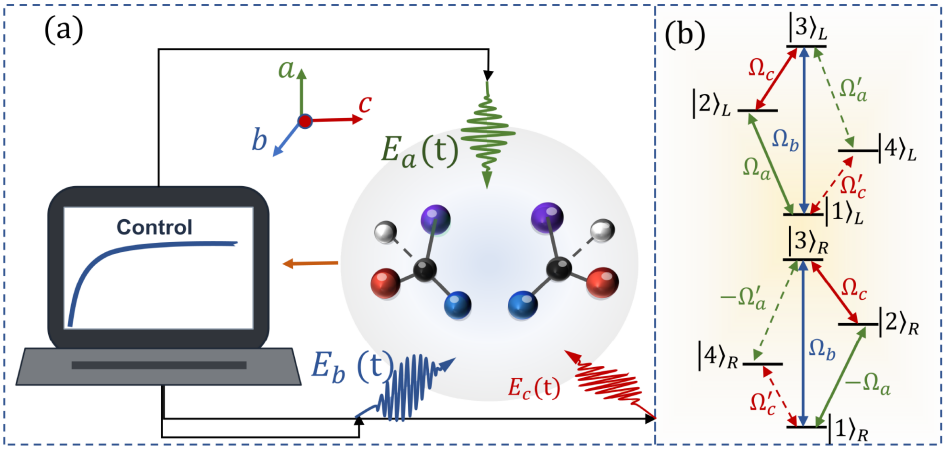


Fig. 1. Schematic illustration of optimized ESST in a four-level chiral-molecule model. (a) Three mutually orthogonal microwave control fields are optimized simultaneously by the constrained multiobjective QOCT procedure. (b) Four-level coupling scheme for the two enantiomers, where the cyclic ESST subsystem $\{|1\rangle, |2\rangle, |3\rangle\}$ is extended by the nearest additional rotational state $|4\rangle$. The sign reversal of the a-type coupling gives rise to enantiomer-dependent pathway interference.

enantiomer is written as

$$H_\chi(t) = H_0 - \sum_{q=a,b,c} M_q^{(\chi)} E_q(t), \tag{1}$$

where $\chi = L, R$ and $H_0 = \sum_{n=1}^{4} E_n |n\rangle\langle n|$ is the field-free Hamiltonian. Throughout this work, we set $\hbar = 1$. The enantiomer-dependent dipole operators are defined as

$$\begin{aligned} M_a^{(L)} &= -M_a^{(R)} = M_a = \mu_{12}|1\rangle\langle 2| + \mu_{34}|3\rangle\langle 4| + \text{H.c.}, \\ M_b^{(L)} &= M_b^{(R)} = M_b = \mu_{13}|1\rangle\langle 3| + \text{H.c.}, \\ M_c^{(L)} &= M_c^{(R)} = M_c = \mu_{23}|2\rangle\langle 3| + \mu_{14}|1\rangle\langle 4| + \text{H.c.} \end{aligned} \tag{2}$$

Here, μ_{mn} denotes the transition dipole matrix element between states $|m\rangle$ and $|n\rangle$, with its sign or phase determined by the adopted phase convention for the rotational states. The enantiomer-dependent sign reversal of the a-type interactions is included explicitly through $M_a^{(L)} = -M_a^{(R)}$. The coherent population dynamics is governed by the time-dependent Schrödinger equation

$$i\frac{\mathrm{d}}{\mathrm{d}t}|\psi_\chi(t)\rangle = H_\chi(t)|\psi_\chi(t)\rangle. \tag{3}$$

The corresponding propagator is denoted by $U_\chi(t, 0)$. Taking the common initial state as $|\psi_\chi(0)\rangle = |1\rangle$, the final transition amplitude and population in state $|f\rangle$ are defined as

$$\begin{aligned} C_\chi(f, T) &= \langle f|U_\chi(T, 0)|1\rangle, \\ P_\chi(f, T) &= |C_\chi(f, T)|^2. \end{aligned} \tag{4}$$

When the spectral bandwidths of the microwave fields are much smaller than the detunings from the additional transitions involving $|4\rangle$, the population of $|4\rangle$ remains negligible and the dynamics is effectively

restricted to the cyclic subsystem $\{|1\rangle, |2\rangle, |3\rangle\}$. In this narrow-band regime, the four-level model reduces to the standard cyclic three-level model. When the bandwidths become comparable to these detunings, $|4\rangle$ can participate in the dynamics, and the full four-level model should be used.

2.2. Multiobjective quantum optimal control method

We now formulate the constrained multiobjective QOCT method used to design the microwave control fields for ESST. Quantum optimal control theory and monotonically convergent optimization algorithms have been extensively developed and reviewed [38–40,48,49]. The simultaneous optimization of multiple quantum objectives has also been considered within multiobjective quantum control [54]. Here, we apply a constrained common-ascent construction to two enantiomer-resolved objectives driven by the same three microwave control fields.

Starting from the common initial state $|1\rangle$, the two enantiomers are required to reach different target states. We denote the target state of enantiomer χ by f_χ, with $f_L = 3$ and $f_R = 2$, corresponding to $|3\rangle$ for the L-handed enantiomer and $|2\rangle$ for the R-handed one. We therefore maximize the two objectives $\mathcal{J}_\chi[\mathbf{E}(t)] = P_\chi(f_\chi, T)$ for $\chi = L, R$, where $\mathbf{E}(t) = \{E_a(t), E_b(t), E_c(t)\}$. This defines a two-objective ESST problem in which a common set of three control fields is optimized to increase $\mathcal{J}_L$ and $\mathcal{J}_R$ simultaneously along the optimization path. Changing the phase of one microwave component by π reverses the handedness associated with these two target rotational states.

Following the monotonic morphing formulation with exact equality constraints on the optimized control fields [52,53], we introduce an artificial variable s to parametrize the optimization path and write each control field as $E_q(s,t)$, with $q = a, b, c$. The initial field corresponds to $E_q(0,t)$, and the field is morphed along the optimization path as s increases. Along this path, the variation of each objective is given by the chain rule as

$$\frac{d\mathcal{J}_\chi}{ds} = \sum_{q=a,b,c} g_{\chi q}(s) = \sum_{q=a,b,c} \int_0^T \frac{\delta \mathcal{J}_\chi}{\delta E_q(s,t)} \frac{\partial E_q(s,t)}{\partial s} dt \geq 0, \tag{5}$$

where $g_{\chi q}(s)$ denotes the contribution of the control field $E_q(s,t)$ to the increase of the objective $\mathcal{J}_\chi$. The functional derivative of each objective with respect to $E_q(t)$ is

$$\frac{\delta \mathcal{J}_\chi}{\delta E_q(t)} = -2\,\mathrm{Im}\left[\langle 1|\mathcal{O}_\chi(T) U_\chi^\dagger(t,0) M_q^{(\chi)} U_\chi(t,0)|1\rangle\right], \tag{6}$$

where $\mathcal{O}_\chi(T) = U_\chi^\dagger(T,0)|f_\chi\rangle\langle f_\chi|U_\chi(T,0)$.

A zero-pulse-area constraint is imposed on each control field to ensure that the optimized fields remain free of dc components throughout the optimization. For each control field $E_q(s,t)$, this constraint is written as

$$h_q[E_q(s,\cdot)] = \int_0^T E_q(s,t) dt = 0. \tag{7}$$

It is preserved along the optimization path by requiring

$$\frac{dh_q}{ds} = \int_0^T \frac{\delta h_q}{\delta E_q(s,t)} \frac{\partial E_q(s,t)}{\partial s} dt = 0. \tag{8}$$

To satisfy Eqs. (5) and (8) simultaneously, the search direction for each control field is constructed as

$$\frac{\partial E_q(s,t)}{\partial s} = S_q(t) \sum_{\substack{\eta=L,R \\ \nu=L,R,0}} g_{\eta q}(s) \left[\Gamma_q^{-1}\right]_{\eta\nu} c_{\nu q}(s,t), \tag{9}$$

where $S_q(t)$ is a shape function that smoothly switches the field update on and off. Here, $c_{\nu q}(s,t) = \delta\mathcal{J}_\nu/\delta E_q(s,t)$ for $\nu = L, R$, and $c_{0q}(s,t) = \delta h_q/\delta E_q(s,t) = 1$. The matrix Γ_q is defined by

$$[\Gamma_q]_{\mu\nu} = \int_0^T c_{\mu q}(s,t) S_q(t) c_{\nu q}(s,t) dt, \qquad \mu,\nu = L, R, 0. \tag{10}$$

Substituting Eq. (9) into Eqs. (5) and (8) gives $d\mathcal{J}_\chi/ds = \sum_{q=a,b,c} g_{\chi q}(s) \geq 0$ for $\chi = L, R$ and $dh_q/ds = 0$ for $q = a, b, c$. Thus, the constructed update is a common ascent direction for the two objectives and preserves the zero-pulse-area constraint.

The same constrained multiobjective procedure is applied in the three-level and four-level descriptions. In the three-level optimization, the dynamics is restricted to the cyclic subsystem formed by $|1\rangle$, $|2\rangle$, and $|3\rangle$, and the resulting fields are then propagated with the four-level Hamiltonian to examine the influence of $|4\rangle$. In the four-level optimization, $|4\rangle$ and its associated couplings are included directly during the search. In both cases, the same objectives $\mathcal{J}_L$ and $\mathcal{J}_R$ and the same zero-pulse-area constraint are used, so that the difference between the two sets of optimized control fields arises from the dynamical model used in the optimization.

2.3. Molecular parameters and bandwidth criterion

To perform numerical simulations, we choose cyclohexylmethanol ($C_7H_{14}O$) as a representative asymmetric-top chiral molecule for microwave ESST [19]. The four rotational states are labeled as $|1\rangle \equiv |1_{01}\rangle$, $|2\rangle \equiv |2_{02}\rangle$, $|3\rangle \equiv |2_{12}\rangle$, and $|4\rangle \equiv |1_{11}\rangle$, where we use the compact notation $|J_{K_a K_c}\rangle$ with the magnetic quantum number M suppressed. Here J is the rotational angular momentum quantum number, while K_a and K_c label the limiting prolate- and oblate-top projections. We set $E_1 = 0$, $E_2 = 2\pi \times 4720$ MHz, $E_3 = 2\pi \times 7059$ MHz, and $E_4 = 2\pi \times 2575$ MHz.

The permanent dipole components of cyclohexylmethanol along the principal axes are $|\mu_a| = 0.4$ D, $|\mu_b| = 1.2$ D, and $|\mu_c| = 0.8$ D. In the reduced four-level model, the molecular couplings are described in terms of effective transition dipole matrix elements. Following the conventional asymmetric-top angular-momentum formalism [12,28], the rotational eigenstates are expanded in the symmetric-top basis, and the corresponding direction-cosine matrix elements are evaluated using Wigner-3j symbols. The resulting effective transition dipole matrix elements incorporate rotational-state mixing and the relevant magnetic-sublevel- and polarization-dependent geometrical factors. For compactness, the magnetic-sublevel indices are not shown explicitly in the reduced-state notation. In a complete M-resolved description, the three orthogonal microwave fields can generate multiple M-resolved coupling pathways [33]. The present four-level model therefore represents a selected reduced coupling network rather than the full set of degenerate magnetic sublevels, and the calculated transfer efficiencies refer to this reduced network rather than to ensemble-averaged efficiencies for the complete M-resolved manifold.

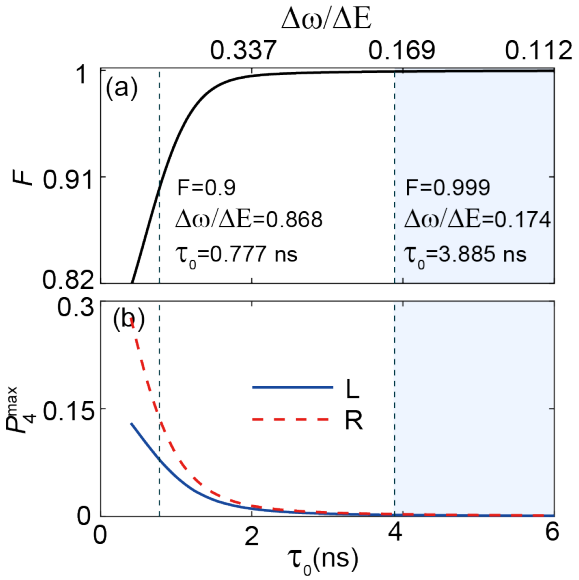


Fig. 2. Bandwidth-induced limitation of the isolated three-level approximation. The analytical control fields are designed in the cyclic three-level model and propagated with the four-level Hamiltonian. (a) Discrimination degree F as a function of the pulse duration τ_0, with the normalized bandwidth $\Delta\omega/\Delta E$ shown on the upper axis. Here, $\Delta\omega = 1/\tau_0$ is the spectral bandwidth of the control field. (b) Maximum transient population of $|4\rangle$ for the two enantiomers.

For this level structure, the additional transitions involving $|4\rangle$ are near the microwave transitions of the cyclic subsystem. The a-type field resonant with $|1\rangle \leftrightarrow |2\rangle$ is detuned from the $|3\rangle \leftrightarrow |4\rangle$ transition by $\Delta E_a = |(E_2 - E_1) - (E_3 - E_4)| = 2\pi \times 236$ MHz. Similarly, the c-type field resonant with $|2\rangle \leftrightarrow |3\rangle$ is detuned from the $|1\rangle \leftrightarrow |4\rangle$ transition by $\Delta E_c = |(E_3 - E_2) - (E_4 - E_1)| = 2\pi \times 236$ MHz. We denote this common detuning scale by ΔE. According to the measured rotational spectrum of cyclohexylmethanol [19], the closest dipole-allowed transition that directly connects the four-level subspace considered here to an additional rotational state outside this subspace is detuned from the corresponding control frequency by approximately $2\pi \times 1994$ MHz. This value is about 8.4 times larger than the $2\pi \times 236$ MHz detuning associated with $|4\rangle$. This separation defines a finite bandwidth range in which the transitions involving $|4\rangle$ can become spectrally relevant while the more distant direct leakage channels remain far off resonance. The four-level model therefore serves as a representative minimal extension of the cyclic three-level model within this range.

To quantify the enantioselective state discrimination associated with $|3\rangle$, we define the discrimination degree as

$$F = P_L(3, T) - P_R(3, T). \tag{11}$$

The value $F = 1$ indicates that the L-handed enantiomer is completely transferred to $|3\rangle$, while the population of the R-handed enantiomer in $|3\rangle$ is fully suppressed. Thus, F measures the state-selective population contrast between the two enantiomers. Figure 2 shows the discrimination degree F and the maximum transient population of $|4\rangle$ as functions of the pulse duration τ_0 of the two-stage analytical

Gaussian control fields [26]. The corresponding normalized bandwidth $\Delta\omega/\Delta E$ is shown on the upper axis, where $\Delta\omega = 1/\tau_0$ is the spectral bandwidth of the control field. The results are obtained by propagating the two-stage analytical control fields with the four-level Hamiltonian. The analytical control fields are designed in the cyclic three-level model and serve as a benchmark for examining the bandwidth-induced limitation of the isolated three-level approximation.

For long pulse durations, the bandwidth is small compared with the detuning scale ΔE, and the maximum transient population of $|4\rangle$ remains negligible. For example, when $\tau_0 > 3.885$ ns, corresponding to the normalized bandwidth $\Delta\omega/\Delta E < 0.174$, the analytical control fields reach near-perfect ESST with $F > 0.999$. As the pulse duration is reduced, $\Delta\omega/\Delta E$ increases, and $|4\rangle$ is off-resonantly driven during the evolution. Meanwhile, the discrimination produced by the analytical control fields drops below the near-perfect value. This result shows that, in the broadband regime, $|4\rangle$ should be included directly in the optimization so that its transient population can be coherently controlled.

This bandwidth dependence naturally separates the optimal-control problem into two regimes. In the narrow-band regime, where $|4\rangle$ remains nearly unpopulated, the cyclic three-level model is sufficient for the optimization. The resulting fields are then tested by four-level propagation. In the broadband regime, however, $|4\rangle$ can be transiently populated and should be included directly in the optimization. We therefore analyze two sets of optimized control fields in the following sections: three-level optimized control fields obtained in the narrow-band regime and four-level optimized control fields designed in the broadband regime.

For the numerical optimal-control calculations, the initial fields are taken as

$$E_q(0,t) = E_{q0} \exp\left[-\frac{(t-T/2)^2}{2\tau_0^2}\right] \cos\left[\omega_q(t-T/2)\right], \qquad q = a, b, c, \tag{12}$$

with center frequencies chosen to be resonant with the corresponding transitions of the cyclic three-level subsystem. Specifically, $\omega_a = 2\pi \times 4720$ MHz, $\omega_b = 2\pi \times 7059$ MHz, and $\omega_c = 2\pi \times 2339$ MHz. The peak amplitudes E_{q0} are chosen such that the area of each Rabi frequency envelope is $\pi/2$, corresponding to a complex pulse area of magnitude $\pi/4$ according to the convention of Ref. [26]. For both optimizations, the same update shape function $S_q(t) = \exp[-(t-T/2)^2/(2\tau_0^2)]$ is used for $q = a, b, c$. The zero-pulse-area condition introduced in Sec. 2.2 is imposed on each control field throughout the optimizations. For the three-level optimization, the pulse duration is $\tau_0 = 5$ ns and the total control duration is $T = 8\tau_0 = 40$ ns. For the four-level optimization, the corresponding parameters are $\tau_0 = 1$ ns and $T = 8$ ns. In both calculations, the control interval is divided into 20000 equal time steps, and the optimization is terminated when both enantiomer-resolved target-state populations exceed 0.999.

3. Even/odd-a pathway interference of the three-level optimized control fields

We begin with the microwave control fields optimized in the cyclic three-level model. This case represents the narrow-band regime identified in Sec. 2.3, where the pulse bandwidth is small compared

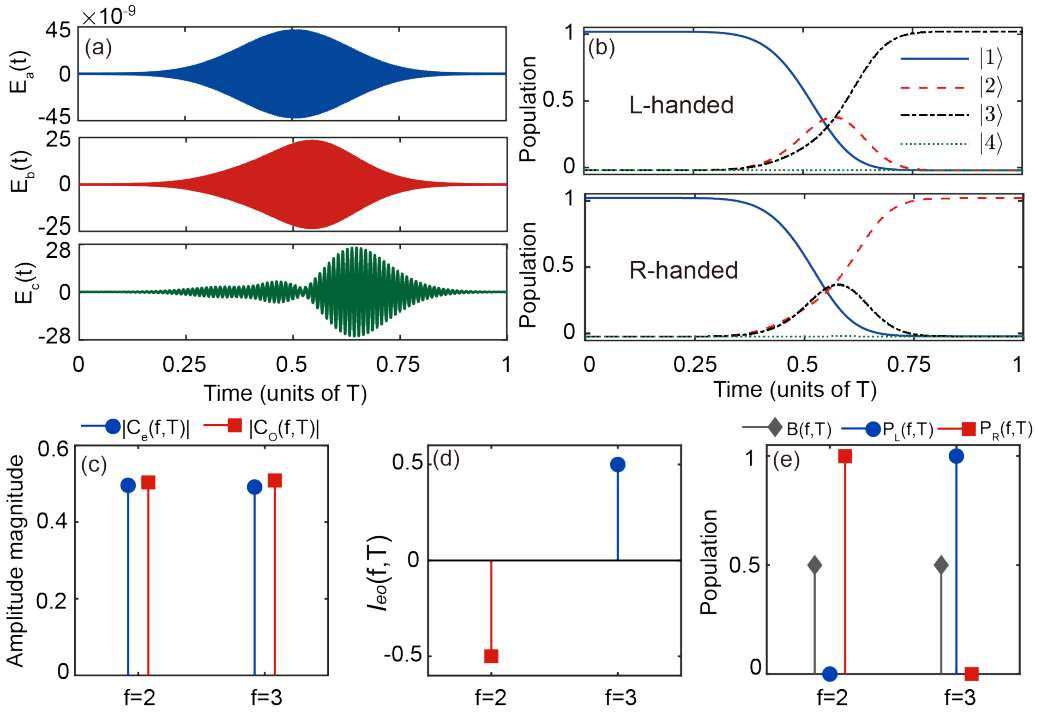


Fig. 3. Three-level optimized microwave control fields and chirality-dependent pathway-interference analysis in the four-level embedding. (a) Optimized microwave control fields obtained in the cyclic three-level model, with amplitudes given in atomic units. (b) Four-level population dynamics for the two enantiomers. (c) Magnitudes of the even-a (enantiomer-symmetric) and odd-a (enantiomer-antisymmetric) pathway-group amplitudes, $|C_e(f,T)|$ and $|C_o(f,T)|$, respectively, for $f = 2$ and $f = 3$. (d) Interference term $I_{eo}(f,T)$ between the even-a and odd-a pathway groups for the two analyzed states. (e) Population reconstruction from $B(f,T)$ and $I_{eo}(f,T)$.

with the detuning scale ΔE and $|4\rangle$ is expected to remain dynamically inactive. We use this case to examine whether the three-level optimized fields remain effective under four-level propagation and to identify the interference mechanism responsible for the resulting ESST.

The three optimized microwave control fields are shown in Fig. 3(a). Propagation of these fields with the four-level Hamiltonian in Eq. (1) gives the population dynamics shown in Fig. 3(b). The population is almost entirely transferred to $|3\rangle$ for the L-handed enantiomer and to $|2\rangle$ for the R-handed enantiomer, while the population of $|4\rangle$ remains negligible during the whole process. This confirms that the three-level optimized control fields remain valid in the four-level model in the present narrow-band regime. To identify the interference mechanism underlying this enantioselective transfer, we analyze the final transition amplitudes by separating the contributions according to the parity of the a-type interaction.

The separation is based on the only enantiomer-dependent sign in the Hamiltonian. In Eq. (1), the enantiomeric difference is represented by the sign reversal of the a-type interaction, while the field-free Hamiltonian and the b- and c-type interactions are the same for the two enantiomers. We therefore write

$$H_\chi(t) = H_{bc}(t) + \sigma_\chi V_a(t), \tag{13}$$

where $H_{bc}(t) = H_0 - M_b E_b(t) - M_c E_c(t)$, $V_a(t) = -M_a E_a(t)$, $\sigma_L = +1$, and $\sigma_R = -1$. In the four-level model, the operator M_a contains both the cyclic transition $|1\rangle \leftrightarrow |2\rangle$ and the additional transition $|3\rangle \leftrightarrow |4\rangle$. Thus the parity classification below counts all sign-changing a-type interactions, whether they occur inside the cyclic subsystem or through the additional coupling.

In the interaction picture with respect to $H_{bc}(t)$, the Dyson expansion gives $C_\chi(f,T) = \sum_{n=0}^{\infty} \sigma_\chi^n A_n(f,T)$ [58,59], where $A_n(f,T)$ collects all contributions containing exactly n interactions with $V_a(t)$, while the evolution generated by $H_{bc}(t)$ is included in the interaction-picture dressing. Terms containing even numbers of a-type interactions are invariant under the enantiomeric sign reversal, whereas those containing odd numbers change sign. Defining $C_e(f,T) = \sum_{n\,\mathrm{even}} A_n(f,T)$ and $C_o(f,T) = \sum_{n\,\mathrm{odd}} A_n(f,T)$, we obtain

$$C_\chi(f,T) = C_e(f,T) + \sigma_\chi C_o(f,T). \tag{14}$$

Here, the labels "even-a" and "odd-a" indicate whether the corresponding contributions contain even and odd numbers of a-type interactions, respectively. Accordingly, C_e is symmetric, whereas C_o is antisymmetric, under the enantiomeric sign reversal of the a-type interaction. This classification does not refer to the spatial parity of the rotational states.

For the numerical analysis, the pathway-group amplitudes are extracted from the propagated amplitudes as $C_e = (C_L + C_R)/2$ and $C_o = (C_L - C_R)/2$. This extraction represents an exact symmetry decomposition of the propagated amplitudes rather than a low-order perturbative approximation. It therefore includes all higher-order pathways generated by the optimized control fields under the four-level Hamiltonian.

The corresponding population in the state $|f\rangle$ can be written as

$$P_\chi(f,T) = B(f,T) + \sigma_\chi I_{eo}(f,T), \tag{15}$$

where $B(f,T) = |C_e(f,T)|^2 + |C_o(f,T)|^2$ is the handedness-independent contribution, while $I_{eo}(f,T) = 2\mathrm{Re}[C_e(f,T)C_o^*(f,T)]$ is the interference term between the even-a and odd-a pathway groups. The sign of $I_{eo}(f,T)$ determines which enantiomer is enhanced in the state $|f\rangle$. A positive value enhances the population of the L-handed enantiomer and suppresses the corresponding population of the R-handed enantiomer, whereas a negative value has the opposite effect.

Figures 3(c)–3(e) illustrate the even/odd-a pathway-interference mechanism for the two target states $f = 2$ and $f = 3$. Figure 3(c) shows that the magnitudes of the even- and odd-a pathway groups are comparable in both states. The ESST is therefore not caused by the dominance of one pathway group over the other, but by their relative phase, i.e., by the sign of $I_{eo}(f,T)$. As shown in Fig. 3(d), $I_{eo}(2,T) < 0$ for the target state $f = 2$ of the R-handed enantiomer, which suppresses $P_L(2,T)$ and enhances $P_R(2,T)$. By contrast, $I_{eo}(3,T) > 0$ for the target state $f = 3$ of the L-handed enantiomer, which enhances $P_L(3,T)$ and suppresses $P_R(3,T)$. Thus, in each target state, the even- and odd-a pathway groups interfere constructively for the desired enantiomer and destructively for the other. This explains why the L-handed enantiomer is transferred to $|3\rangle$, whereas the R-handed one is transferred to $|2\rangle$ as shown in Fig. 3(b).

Figure 3(e) further verifies this interpretation by reconstructing the final populations from $B(f,T)$ and $I_{eo}(f,T)$. For each target state f, the gray stem markers give the handedness-independent contribution $B(f,T)$, while the blue and red stem markers give the reconstructed populations $P_L(f,T)$ and $P_R(f,T)$ obtained from Eq. (15). The reconstruction reproduces the final populations obtained from direct four-level propagation. The optimized control fields therefore do not act as an incoherent population filter. Instead, they organize the final transition amplitudes so that the same pair of even- and odd-a pathway groups interferes constructively for the desired enantiomer and destructively for the other one. These results show that, for the present narrow-band regime, the three-level optimized control fields remain effective after four-level propagation, and the observed ESST arises from constructive and destructive interference between pathway groups with opposite enantiomeric signs.

4. Even/odd-a pathway interference with transient fourth-state participation

We now turn to the broadband regime, in which the fourth state $|4\rangle$ cannot be neglected during the control process. In contrast to the fields discussed in Sec. 3, the microwave control fields considered here are optimized directly in the four-level model. In this way, the transient participation of $|4\rangle$ is incorporated into the search, so that its population can be coherently controlled while the desired ESST is maintained.

Figure 4(a) shows the three microwave control fields optimized in the four-level model. Compared with the three-level optimized fields in Fig. 3(a), the four-level optimized fields show stronger temporal modulation and larger peak amplitudes, reflecting the inclusion of $|4\rangle$ and its associated couplings during the optimization. The corresponding population dynamics is shown in Fig. 4(b). The optimized control fields realize the desired ESST, transferring the L-handed enantiomer to $|3\rangle$ and the R-handed enantiomer to $|2\rangle$. The inset displays the population of $|4\rangle$. In contrast to the three-level optimized fields, the four-level optimized fields generate an appreciable transient population in $|4\rangle$ during the control process. This population subsequently decreases as the system is driven toward the target-state manifold. Thus, $|4\rangle$ participates in the intermediate dynamics of the optimized ESST process, but it does not serve as a separate final population channel.

The even/odd-a pathway analysis introduced in Sec. 3 remains applicable to the present four-level optimized fields. This analysis allows us to examine whether the transient participation of $|4\rangle$ changes the interference structure responsible for the final ESST. Figures 4(c)–4(e) illustrate the even/odd-a pathway-interference mechanism for the two target states, $f = 2$ and $f = 3$. As shown in Fig. 4(c), the magnitudes of the even- and odd-a pathway groups are comparable in both target states. Thus, although $|4\rangle$ is transiently populated during the dynamics, the ESST is still controlled by the relative phase between the two pathway groups rather than by an imbalance in their magnitudes.

Figure 4(d) shows that the interference term has the sign pattern required for ESST: $I_{eo}(2,T) < 0$ and $I_{eo}(3,T) > 0$. According to Eq. (15), this sign pattern enhances the desired enantiomeric population in each

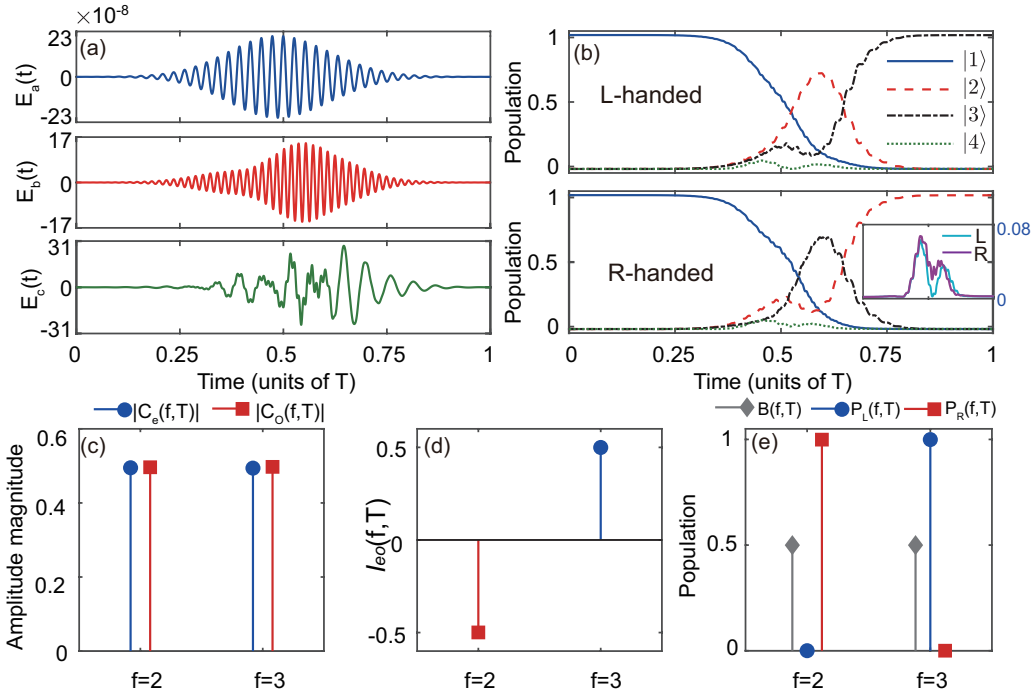


Fig. 4. Four-level optimized microwave control fields and chirality-dependent pathway-interference analysis. (a) Optimized microwave control fields obtained in the four-level model, with amplitudes given in atomic units. (b) Four-level population dynamics for the two enantiomers. The inset shows the transient population of $|4\rangle$. (c) Magnitudes of the even-a (enantiomer-symmetric) and odd-a (enantiomer-antisymmetric) pathway-group amplitudes, $|C_e(f,T)|$ and $|C_o(f,T)|$, respectively, for the target states $f = 2$ and $f = 3$. (d) Interference term $I_{eo}(f,T)$ between the even-a and odd-a pathway groups for the two target states. (e) Population reconstruction from $B(f,T)$ and $I_{eo}(f,T)$.

target state and suppresses the other one. Figure 4(e) shows the corresponding population reconstruction from $B(f,T)$ and $I_{eo}(f,T)$. The reconstructed populations agree with those obtained from direct four-level propagation. These results indicate that the transient participation of $|4\rangle$ modifies the intermediate population dynamics without changing the even/odd-a interference structure responsible for the final ESST. Thus, the four-level optimization coherently controls the transient fourth-state population while preserving the pathway-interference mechanism identified in the narrow-band three-level optimized case.

From an experimental perspective, the peak amplitudes of the three-level optimized fields range from 120 to 211 V/cm, whereas those of the four-level optimized fields range from 0.757 to 1.43 kV/cm. Three mutually orthogonal and phase-controlled microwave fields have already been implemented in molecular-beam ESST experiments [21], and microwave fields of about 1.4 kV/cm have been generated in a molecular-beam apparatus [60]. Short microwave excitation pulses on the nanosecond timescale have also been used in broadband rotational spectroscopy [61]. These experimental capabilities suggest that the present field amplitudes and nanosecond control durations are experimentally accessible in principle.

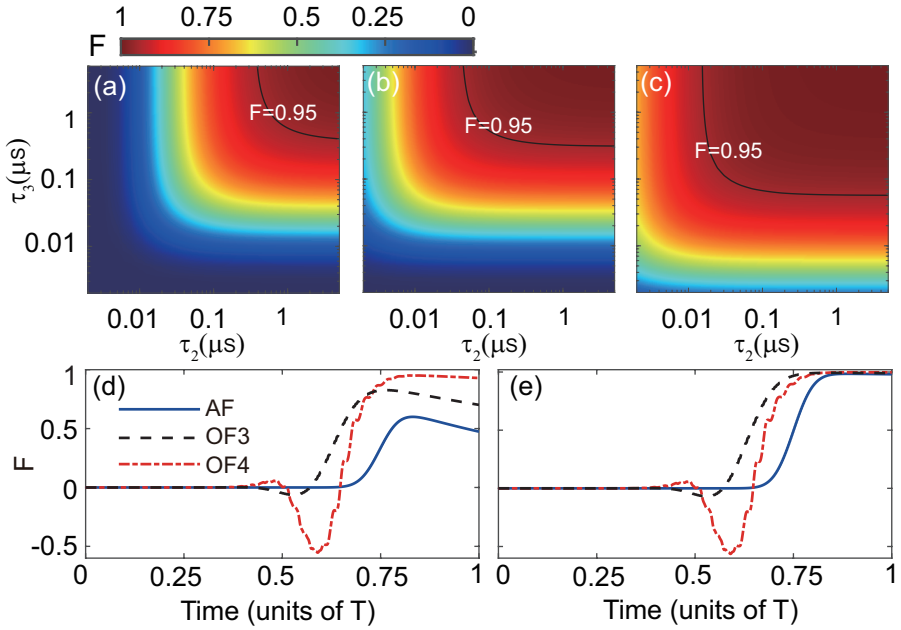


Fig. 5. Influence of dissipative relaxation on ESST. Final discrimination degree F as a function of τ_2 and τ_3 for (a) the two-stage analytical control fields (AF), (b) the three-level optimized control fields (OF3), and (c) the four-level optimized control fields (OF4). The black contour line corresponds to $F = 0.95$. Time evolution of F for (d) $\tau_2 = \tau_3 = 50$ ns and (e) $\tau_2 = \tau_3 = 2000$ ns, respectively.

5. Influence of dissipative relaxation

The preceding sections focused on the coherent control mechanism. In a gas-phase or molecular-beam implementation, however, rotational relaxation can reduce the interference contrast responsible for ESST. To examine this effect, we compare the two-stage analytical control fields, the three-level optimized control fields, and the four-level optimized control fields under the same dissipative four-level dynamics. For the two-stage analytical protocol, the pulse duration is $\tau_0 = 5$ ns, with a total control duration of 80 ns. For comparison, the total control durations of the three-level and four-level optimized fields are 40 and 8 ns, respectively, as specified in Sec. 2.3.

The density operator for each enantiomer is propagated according to the Lindblad master equation [62]

$$\frac{\mathrm{d}\rho_\chi}{\mathrm{d}t} = -\mathrm{i}[H_\chi(t), \rho_\chi] + \mathcal{L}[\rho_\chi], \qquad \chi = L, R, \tag{16}$$

where $H_\chi(t)$ is the four-level Hamiltonian in Eq. (1). The dissipative part is written as

$$\mathcal{L}[\rho] = \sum_{m,n} \frac{\gamma_{mn}}{2} \left(2\sigma_{mn}\rho\sigma_{mn}^\dagger - \sigma_{mn}^\dagger\sigma_{mn}\rho - \rho\sigma_{mn}^\dagger\sigma_{mn}\right), \tag{17}$$

where $\sigma_{mn} = |m\rangle\langle n|$ denotes the jump operator for the transition $|n\rangle \to |m\rangle$, and γ_{mn} is the corresponding relaxation rate.

We include relaxation channels from $|3\rangle$ to $|1\rangle$, $|2\rangle$, and $|4\rangle$, and from $|2\rangle$ to $|1\rangle$. To account for the nondegenerate transition frequencies, the branching rates are obtained by normalizing the Einstein A coefficients as $\gamma_{mn} = \tau_n^{-1}\omega_{nm}^3|\mu_{mn}|^2 / \sum_{k\in\mathcal{L}_n} \omega_{nk}^3|\mu_{kn}|^2$, where $\omega_{nm} = E_n - E_m$, τ_n is the total phenomenological relaxation time assigned to the upper state $|n\rangle$ within the present model, and $\mathcal{L}_n$ denotes the set of

included lower states connected to $|n\rangle$ by allowed electric-dipole transitions. This gives $\gamma_{13} = 0.9465/\tau_3$, $\gamma_{23} = 0.0400/\tau_3$, and $\gamma_{43} = 0.0135/\tau_3$, together with $\gamma_{12} = 1/\tau_2$. The relaxation times τ_2 and τ_3 are varied to compare the three control protocols under the same dissipative conditions. No separate lifetime τ_4 is assigned to $|4\rangle$, because $|4\rangle$ lies below $|2\rangle$ and $|3\rangle$ and is either negligibly or only transiently populated during the control dynamics considered here. Possible relaxation from $|4\rangle$ is therefore neglected in the present minimal dissipative model.

Figures 5(a)–5(c) show the final discrimination degree F as a function of τ_2 and τ_3 for the three sets of control fields. The two-stage analytical control fields give the smallest high-discrimination region, whereas the three-level optimized control fields enlarge this region. The four-level optimized control fields provide the largest high-discrimination region, as indicated by the $F = 0.95$ contour, and thus exhibit the strongest tolerance to dissipative relaxation.

The different sensitivities can be understood mainly from the control time required to achieve ESST. The analytical control fields are implemented in two separate stages and must remain narrow band in order to suppress unwanted transitions, leading to the longest total control duration. The three-level optimized control fields are not divided into two stages, but they are still designed in the narrow-band regime and therefore require an intermediate control time. In contrast, the four-level optimized control fields are obtained in the broadband regime, where the fourth state is included directly in the optimization. This allows a shorter control time while still achieving the desired ESST.

The time-dependent discrimination degree shown in Figs. 5(d) and 5(e) further supports this interpretation. Owing to their shorter control duration, the four-level optimized control fields achieve ESST before relaxation has sufficient time to degrade the coherent pathway interference. The three-level optimized control fields show an intermediate behavior, while the two-stage analytical control fields are most strongly affected by dissipation because of their longer interaction time. Thus, the improved dissipative robustness of the four-level optimized control fields does not come from a different origin of ESST, but from a faster realization of the same even/odd-a pathway-interference mechanism under dissipative dynamics.

6. Conclusion

In summary, we theoretically studied ESST in a four-level rotational model for a chiral molecule. By embedding the cyclic three-level subsystem into a larger Hilbert space containing the nearest relevant fourth rotational state, we examined the bandwidth-induced limitation of the isolated three-level approximation. In the narrow-band regime, the fourth state remains nearly inactive and the cyclic three-level model gives an adequate description. In the broadband regime, however, the fourth state can participate transiently, so the control fields should be designed in the enlarged four-level model.

Using a constrained multiobjective QOCT method, we optimized three microwave control fields in both the three-level and four-level descriptions. The three-level optimized control fields remain effective after four-level propagation when the bandwidth is sufficiently narrow. By contrast, the four-level optimized control fields coherently control the transient population of $|4\rangle$ and return the population to the

target-state manifold, thereby realizing faster ESST. This shows that the fourth state is not merely an unwanted leakage channel, but can be coherently managed by broadband optimization.

The coherent mechanism was clarified by decomposing the transition amplitudes into even- and odd-a pathway groups. For both sets of optimized control fields, the even-a contribution is common to the two enantiomers, whereas the odd-a contribution changes sign. Their interference enhances the desired enantiomeric population in each target state and suppresses the other one. Lindblad simulations further show that the faster four-level optimized control fields have stronger tolerance to dissipative relaxation. These results suggest that broadband four-level optimization can improve the speed and dissipative robustness of microwave ESST while preserving the same even/odd-a pathway-interference mechanism.

Acknowledgments

This work was supported by the National Natural Science Foundation of China (NSFC) under Grant No. 12275033 and the Natural Science Foundation of Hunan Province under Grant No. 2022JJ30582.

References

[1] Barron L D 2004 *Molecular Light Scattering and Optical Activity* 2nd edn (Cambridge: Cambridge University Press)

[2] Quack M 2002 *Angew. Chem. Int. Ed.* **41** 4618

[3] Patterson D, Schnell M and Doyle J M 2013 *Nature* **497** 475

[4] Patterson D and Doyle J M 2013 *Phys. Rev. Lett.* **111** 023008

[5] Ye C, Zhang Q, Chen Y Y and Li Y 2019 *Phys. Rev. A* **100** 033411

[6] Xu X W, Ye C, Li Y and Chen A X 2020 *Phys. Rev. A* **102** 033727

[7] Chen Y Y, Cheng J J, Ye C and Li Y 2022 *Phys. Rev. Research* **4** 013100

[8] Cai M R, Ye C, Dong H and Li Y 2022 *Phys. Rev. Lett.* **129** 103201

[9] Zou F, Chen Y Y, Liu B and Li Y 2022 *Opt. Express* **30** 31073

[10] Kang Y H, Lin Z P, Yang J Q, Song J and Xia Y 2023 *Phys. Rev. A* **107** 053714

[11] Ye C, Mu X, Sun Y, Fu L and Zhang X 2024 *Phys. Rev. A* **109** 023114

[12] Leibscher M, Giesen T F and Koch C P 2019 *J. Chem. Phys.* **151** 014302

[13] Král P and Shapiro M 2001 *Phys. Rev. Lett.* **87** 183002

[14] Li Y and Bruder C 2008 *Phys. Rev. A* **77** 015403

[15] Jia W Z and Wei L F 2010 *J. Phys. B: At. Mol. Opt. Phys.* **43** 185402

[16] Král P, Thanopulos I, Shapiro M and Cohen D 2003 *Phys. Rev. Lett.* **90** 033001

[17] Eibenberger S, Doyle J and Patterson D 2017 *Phys. Rev. Lett.* **118** 123002

[18] Pérez C, Steber A L, Domingos S R, Krin A, Schmitz D and Schnell M 2017 *Angew. Chem. Int. Ed.* **56** 12512

[19] Pérez C, Steber A L, Krin A and Schnell M 2018 *J. Phys. Chem. Lett.* **9** 4539

[20] Lee J, Bischoff J, Hernandez-Castillo A O, Sartakov B, Meijer G and Eibenberger-Arias S 2022 *Phys. Rev. Lett.* **128** 173001

[21] Lee J, Abdiha E, Sartakov B G, Meijer G and Eibenberger-Arias S 2024 *Nat. Commun.* **15** 7441

[22] Vitanov N V and Drewsen M 2019 *Phys. Rev. Lett.* **122** 173202

[23] Cheng J J, Ye C and Li Y 2023 *J. Chem. Phys.* **158** 164303

[24] Wu J L, Wang Y, Song J, Xia Y, Su S L and Jiang Y Y 2019 *Phys. Rev. A* **100** 043413

[25] Wu J L, Wang Y, Han J X, Wang C, Su S L, Xia Y, Jiang Y Y and Song J 2020 *Phys. Rev. Applied* **13** 044021

[26] Guo Y, Gong X, Ma S S and Shu C C 2022 *Phys. Rev. A* **105** 013102

[27] Gong X, Guo Y, Wang C Z, Luo X B and Shu C C 2022 *Phys. Chem. Chem. Phys.* **24** 18722

[28] Hong Q Q, Song X J, Xu L and Shu C C 2026 *ChemPhysChem* **27** e202500705

[29] Ye C, Zhang Q, Chen Y Y and Li Y 2019 *Phys. Rev. A* **100** 043403

[30] Cheng J J, Chen Y Y, Li Y and Zhang L 2023 *Phys. Rev. A* **107** 013718

[31] Liu B, Li Y, Ye C and Sun C P 2024 *Opt. Express* **32** 28282

[32] Zou F, Li Y and Zhang P 2024 *J. Phys. Chem. Lett.* **15** 10554

[33] Leibscher M, Pozzoli E, Pérez C, Schnell M, Sigalotti M, Boscain U and Koch C P 2022 *Commun. Phys.* **5** 110

[34] Chen T, Li H, Shi X S, Imbrogno J and Zhao D 2024 *J. Am. Chem. Soc.* **146** 14433

[35] Xu T, Cao L, An S H, Liu X W, Li Z and Lai Z P 2025 *Nat. Commun.* **16** 7803

[36] Stefanatos D, Thanopulos I and Paspalakis E 2025 *Phys. Rev. A* **112** 023116

[37] Han M P, Fu L and Ye C 2026 *Phys. Rev. A* **113** 043117

[38] Rabitz H, de Vivie-Riedle R, Motzkus M and Kompa K 2000 *Science* **288** 824

[39] Werschnik J and Gross E K U 2007 *J. Phys. B: At. Mol. Opt. Phys.* **40** R175

[40] Brif C, Chakrabarti R and Rabitz H 2010 *New J. Phys.* **12** 075008

[41] Tian J Z, Du T Y, Liu Y, Liu H B, Jin F Z, Said R S and Cai J M 2019 *Phys. Rev. A* **100** 012110

[42] Ansel Q, Dionis E, Arrouas F, Peaudecerf B, Guérin S, Guéry-Odelin D and Sugny D 2024 *J. Phys. B: At. Mol. Opt. Phys.* **57** 133001

[43] Dong X, Cao X, Li W L, Zhang G F, Peng Z H and Wu R B 2025 *Phys. Rev. Applied* **23** 044045

[44] Tang R Q, Hou Y J, Du Z Y, Xu Z Y, Chen Y Q, Li Z K and Peng X H 2026 *Chin. Phys. B* **35** 060302

[45] Liu R, Yang X D, Lin Y H, Lu Y and Li J 2025 *Chin. Phys. Lett.* **42** 080601

[46] Chakrabarti R, Wu R B and Rabitz H 2008 *Phys. Rev. A* **77** 063425

[47] Fan L B and Guo Y 2026 *J. Phys. B: At. Mol. Opt. Phys.* **59** 165501

[48] Zhu W, Botina J and Rabitz H 1998 *J. Chem. Phys.* **108** 1953

[49] Maday Y and Turinici G 2003 *J. Chem. Phys.* **118** 8191

[50] Reich D M, Ndong M and Koch C P 2012 *J. Chem. Phys.* **136** 104103

[51] Lapert M, Tehini R, Turinici G and Sugny D 2009 *Phys. Rev. A* **79** 063411

[52] Shu C C, Ho T S, Xing X and Rabitz H 2016 *Phys. Rev. A* **93** 033417

[53] Shu C C, Ho T S and Rabitz H 2016 *Phys. Rev. A* **93** 053418

[54] Shu C C, Dong D, Petersen I R and Henriksen N E 2017 *Phys. Rev. A* **95** 033809

[55] Guo Y, Dong D and Shu C C 2018 *Phys. Chem. Chem. Phys.* **20** 9498

[56] Guo Y, Luo X B, Ma S and Shu C C 2019 *Phys. Rev. A* **100** 023409

[57] Guo Y, Ma S S and Shu C C 2024 *Chin. Phys. B* **33** 024203

[58] Dyson F J 1949 *Phys. Rev.* **75** 486

[59] Kalev A and Hen I 2021 *New J. Phys.* **23** 103035

[60] Merz S, Vanhaecke N, Jäger W, Schnell M and Meijer G 2012 *Phys. Rev. A* **85** 063411

[61] Park G B and Field R W 2015 *J. Mol. Spectrosc.* **312** 54

[62] Lindblad G 1976 *Commun. Math. Phys.* **48** 119